

THE H₂ VELOCITY FIELD IN HERBIG-HARO 7-11

JOHN S. CARR

Department of Astronomy, Ohio State University, 174 West 18th Avenue, Columbus, OH 43210

Received 1992 July 24; accepted 1992 September 28

ABSTRACT

Fabry-Perot images of the H₂ 1–0 S(1) emission line in Herbig-Haro 7-11 have been obtained with a velocity resolution of 25 km s^{−1} and a spatial resolution of 1''. The H₂ line profiles peak at lower (absolute) radial velocity than the atomic lines and have smaller line widths (FWHM). However, the H₂ profiles have weak high-velocity wings, and the full width at zero intensity velocities are similar to those of the atomic lines. In the vicinity of HH 11, the velocity extent of the H₂ emission is greater than 200 km s^{−1}. It is suggested that the weak emission near HH 11 may be produced by H₂ reformation pumping in fast shocks and that the extremely high velocity CO observed in the same region could have a similar origin. The H₂ emission in HH 7 has the velocity field expected for a radiating bow shock, with strong H₂ emission at the apex of the bow shock. It is suggested that the H₂ emission from HH 7 consists of two components: (1) a magnetic precursor in a high-velocity (~100 km s^{−1}) J-shock which produces most of the H₂ emission, and (2) a postshock component that is responsible for the weak high-velocity emission. The postshock component could be reformation pumping or emission from H₂ that has survived dissociation in the shock front. A theoretical bow shock with a simple parameterized model for the magnetic precursor is presented to explain the observed velocity field in HH 7. J-shocks with magnetic precursors are the most attractive explanation for the combined optical and infrared data, although detailed theoretical calculations of such shocks are required.

Subject headings: ISM: individual (HH 7-11) — ISM: kinematics and dynamics — stars: pre-main-sequence

1. INTRODUCTION

The optical emission line spectrum from Herbig-Haro (HH) objects is understood to originate in the cooling regions behind shock fronts. These shocks are a result of the interaction of high-velocity outflows from young stellar objects with the surrounding interstellar medium, though the details of how the shocks are formed are still not fully understood. Our understanding of HH objects has been based primarily on optical and ultraviolet data. Infrared H₂ line emission has been known to be associated with a number of HH objects since first observed by Elias (1980). Measurements of H₂ line ratios indicate thermal excitation (Elias 1980; Schwartz, Cohen, & Williams 1987; Wilking et al. 1990) which is consistent with the shock nature of HH objects, but more detailed information has been limited until recently.

It is important to understand the origin of the H₂ emission, since, in at least some HH objects, molecular emission could be a significant cooling process that may have impact on the shock physics and hence our understanding of HH objects. It is necessary not only to understand the processes responsible for producing H₂ emission, but also the relationship between the hot atomic and molecular gases, e.g., whether or not the same shocks can explain the atomic and H₂ emission. The answers to these questions may well differ among HH objects. Studies of H₂ emission in HH objects may also prove useful for understanding shocks in interstellar molecular gas in general. In spite of the amount of observational and theoretical work, the best studied interstellar shock, that of the OMC-1 outflow, has no agreed upon interpretation (Hollenbach, Chernoff, & McKee 1989). Studies of shocked molecular gas in HH objects offer some advantages, including smaller and more localized shocks, better known geometries and orientations, and low extinction, which permits the use of both infrared and optical diagnostics of the shocked gas.

The development of infrared cameras has made it possible to image the H₂ emission in HH objects with high spatial resolution, permitting the determination of the morphology of the hot molecular gas and detailed spatial comparisons with the optical atomic emission (e.g., Schwartz et al. 1988; Hartigan, Curiel, & Raymond 1989; Stapelfeldt et al. 1991). In some cases the H₂ emission shows a fair spatial coincidence with the optical, but in other cases the distributions are dissimilar. Velocity information on the H₂ lines was lacking until recently, when Zinnecker et al. (1989) obtained large-beam, velocity resolved spectra of the 1–0 S(1) line in several HH objects. In general, the radial velocities of the 1–0 S(1) lines are lower and the line widths smaller than those of the optical lines.

While narrow-band images of the 1–0 S(1) line are useful for studying the morphology of the H₂ emission, they do not yield information on either the dynamics or the excitation of the gas, both of which are essential to understand the physics of the shocks. Infrared techniques have now reached the point where it is possible to obtain spatially resolved data on both the intensities and velocity profiles for multiple H₂ transitions, which is the type of data required to discriminate among likely H₂ emission mechanisms operating in HH objects. To further our understanding of the dynamics of the molecular gas, a program of high-resolution spectral imaging of H₂ emission in HH objects was initiated. In this paper, a study of the velocity field of H₂ gas in the HH 7-11 region is presented.

HH 7-11 are a linear string of HH objects located in the blue lobe of a bipolar CO outflow. The presumed driving star for this outflow is the infrared source SVS 13. HH 7-11 are particularly low excitation HH objects. Comparisons of atomic line intensity ratios with planar shock models indicate shock velocities less than 30 km s^{−1}, yet the observed line widths are greater than 100 km s^{−1} (Hartigan, Raymond, & Hartmann 1987; Böhm & Solf 1990). The velocity field of HH 7-11 has

been studied in [S II] and H α by Solf & Böhm (1987). All of the HH objects have radial velocities of approximately -50 km s^{-1} with the notable exception of HH 11, which has a radial velocity of -180 km s^{-1} . This HH group is a source of strong molecular hydrogen emission, and a correlation in the spatial distribution of the optical atomic and infrared H $_2$ emission is seen in HH 7, 8, and 10 (Hartigan et al. 1989; Stapelfeldt et al. 1991).

2. DATA

2.1. Observations

The observations of HH 7-11 were made during three nights in 1988 October on the 3.8 m United Kingdom Infrared Telescope. IRCAM, a near-infrared camera with a SBRC 62×58 InSb array, was used with a image scale of $1''.2$ per pixel. The images were taken through a Fabry-Perot (FP) etalon placed in the collimated beam. A gap-scanning etalon with a velocity resolution of 25 km s^{-1} and a free spectral range of 885 km s^{-1} was used in the 338th order. A 1% narrow-band filter centered on the H $_2$ $v = 1-0$ S(1) line at $2.122 \mu\text{m}$ was used for order sorting along with a broad-band K filter for additional blocking. The S(1) filter does pass nearby orders. These orders include some OH sky emission lines which were removed by the sky subtraction.

The field of view included the entire HH 7-11 chain and the infrared source SVS 13. At each etalon spacing four frames were obtained in the order object-sky-sky-object, with an integration time of 100 s per frame. Data were taken over a velocity range of about 350 km s^{-1} at 12 km s^{-1} increments; about one-third of the velocity settings were repeated. A calibration ring image at a fixed FP setting was taken periodically during the night by diffusing a krypton lamp in the beam. The calibration rings provide a measure of drift in the wavelength response of the etalon. The seeing during these observations was less than or equal to the pixel size of $1''.2$.

In order to determine phase-correction constants and the wavelength calibration, calibration cubes were taken by scanning the FP in 12 km s^{-1} steps over a free spectral range while observing a calibration lamp. Calibration cubes with both krypton ($2.117127 \mu\text{m}$) and argon (2.099184 and $2.133871 \mu\text{m}$) lamps were obtained. Since the sky background at this resolution is too faint for use as a flat field, a set of flat fields was obtained on the late afternoon sky by scanning the FP in equally spaced intervals over a free spectral range.

2.2. Data Reduction

The data were reduced and analyzed using the ZODIAC reduction package with software routines written by J. Bland and G. Cecil, following procedures used for optical spectral imaging (Bland & Tully 1989). The nearest sky frame was subtracted from each on-source frame. The acquisition of a sky frame for each source frame proved crucial due to the presence of rings from OH sky emission lines and a variable dark current. Bad pixels were corrected by taking the median of neighboring pixels. The daytime sky flat fields also contained rings from OH lines at a very low level. By summing frames over exactly one order, the rings were effectively removed, leaving a single high signal-to-noise flat field. This flat-field frame showed no residual OH rings to a level of less than 0.4%. After flat-fielding each source frame, a residual sky brightness level was subtracted by measuring the mean level in regions of the field with no H $_2$ emission. Each frame was spatially aligned

by referencing to the infrared source SVS 13. The brightness of SVS 13 was measured as a monitor of transparency and seeing changes, and some data from the third night were eliminated due to the presence of thin clouds. Accurate photometry of the point source was not possible because the large pixel size ($1''.2$) did not sample the seeing, but the measured rms brightness variation in SVS 13 was about 10%. Frames recorded at the same FP spacing were then averaged, and all frames were ordered by FP spacing into a three-dimensional data cube in preparation for phase correction and further analysis.

The phase correction parameters were measured by fitting paraboloids to the krypton and argon calibration cubes. The measured curvature of the phase surface gave a velocity shift across the array of $0.2582r^2 \text{ (km s}^{-1}\text{)}$, where r is the radial distance in pixels from the center of the optical axis. The velocity increment per frame was 11.89 km s^{-1} . The measured accuracy of the phase surface and wavelength scale give a velocity uncertainty of 2 km s^{-1} . However, other errors introduce larger uncertainties for individual frames and pixels. One source of error is wavelength drift in the FP, which was monitored during the observations with periodic calibration rings. A slow drift was observed each night. Rather than resampling the data, an average zero point was taken for all the data; the worst case deviation, either within a night or between nights, was 6 km s^{-1} , equal to one-half of the sampling interval. A random error is introduced by the spatial registration of the frames: in the nonphase corrected frames, the wavelength of a pixel depends upon its position in the array, and translation of the array introduces a wavelength shift that depends upon the magnitude of the spatial shift and the radial position of the pixel. For emission observed *farthest* from the center of the array, this produces an average error of about 6 km s^{-1} with a maximum of about 13 km s^{-1} . Hence, the typical relative velocity uncertainty of a selected point (x, y, v) in the data cube is about 8 km s^{-1} .

3. RESULTS

The reduced data form a data cube of H $_2$ line profiles in the HH 7-11 region with a spatial resolution of $1''.2$ and a velocity resolution of 25 km s^{-1} . The velocity coverage in each pixel is about 350 km s^{-1} , though the central velocity shifts from about 75 km s^{-1} at the center of the field to about -125 km s^{-1} at the position of HH 11. All the velocities in this paper refer to the local standard of rest (LSR). The LSR velocity of the quiescent molecular cloud in which SVS 13 is located is about 8 km s^{-1} .

Figure 1 shows an integrated flux map of the $1-0$ S(1) line derived from the data cube. The infrared source SVS 13 appears in the upper right corner of the field. The brightest regions of H $_2$ emission correspond to the optical HH objects 7, 8, and 10. The map in Figure 1 agrees well with the narrow-band H $_2$ images of Hartigan et al. (1989) and Stapelfeldt et al. (1991), although the signal-to-noise ratio is lower since many velocity channels must be summed to recover the total flux. Some of the H $_2$ emission present in the narrow-band images nearest SVS 13 is absent in Figure 1 because the emission has been phase-shifted outside of the velocity coverage.

Hartigan et al. (1989) and Stapelfeldt et al. (1991) have shown a general spatial correlation between the atomic and H $_2$ emission in HH 7-11, but there are differences in the exact morphology; differences also exist in the spatial distribution of different atomic lines (Hartigan et al. 1989). Weak H $_2$ emission is present at HH 9 and to the immediate west of HH 11. The

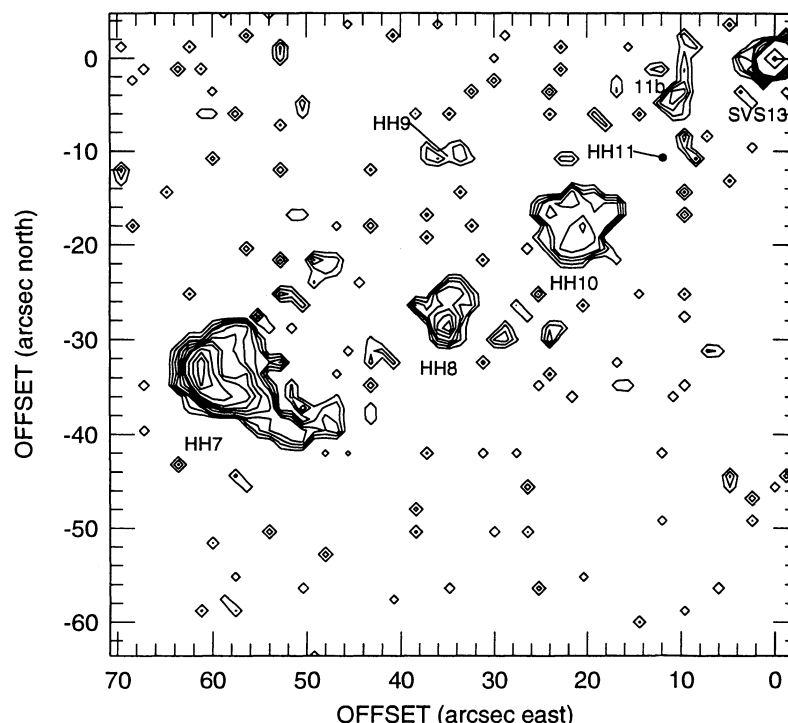


FIG. 1.—Map of the velocity integrated 1–0 $S(1)$ line emission obtained from the data cube. The contour levels are 1, 2, 3, 4, 6, 8, 10, 16, 20, 24, 80, and 160 σ

H₂ emission to the north of HH 11, apparently has no atomic counterpart (Stapelfeldt et al. 1991). In this paper, the knot of H₂ emission directly to the west of HH 11 is referred to as HH 11 and the emission to the north as HH 11b, following Stapelfeldt et al. (1991). There is also patchy H₂ emission in the regions between the HH knots which is apparent when the data in Figure 1 are binned to lower spatial resolution. This interknot emission is also seen in H α and [S II] images (Solf & Böhm 1987).

3.1. Integrated Profiles

We first examine spatially integrated profiles for the H₂ emission. Such profiles are useful for increasing the signal-to-noise ratio of weak emission features and for comparing the data to large aperture optical and infrared spectra. The integrated profiles for various HH objects and regions are shown in Figure 2. For HH 7, 8, and 10 the area of integration is within the first intensity contour shown in Figure 1, with the exclusion of the southwest “tail” in HH 7. A rectangular box was used for HH 9, HH 11, and HH 11b with areas of 14, 17, and 58 square arcsec, respectively. The spectrum marked “diffuse” includes all of the region between HH 7 and HH 10 (excluding HH 8) and covers an area of 815 square arcsec. The velocity information is incomplete for some profiles due to the phase shift across the array: the HH 8 spectrum is incomplete for velocities less than -100 km s^{-1} , and the spectra for HH 11 and 11b have incomplete coverage for velocities greater than 40 and -50 km s^{-1} , respectively. The spectra were smoothed with a $(1/4-1/2-1/4)$ Hanning window, and no attempt was made to deconvolve the Lorentzian instrumental profile from the data.

The H₂ profiles from HH 7 to HH 10 are fairly similar. The emission peaks fall in the range -10 to -20 km s^{-1} , and line widths (FWHM) are $40-50 \text{ km s}^{-1}$. This corresponds to a

blueshift of $20-30 \text{ km s}^{-1}$ with respect to the molecular cloud velocity. The lowest absolute radial velocity and smallest line width is found for the faint emission associated with HH 9. The profile for HH 7 shows a blueshifted wing or shoulder that extends to about -100 km s^{-1} . HH 8 and HH 10 have more symmetrical profiles with the blue wing perhaps slightly stronger than the red. The average profile of the diffuse H₂ emission in the regions between HH 7, 8, and 10 differs from that of the individual emission knots in having a very prominent blue wing extending to at least -100 km s^{-1} . A similar wing is present in the HH 11b spectrum. The emission in HH 11b appears to peak at -45 km s^{-1} , but some emission at more positive velocities is lost due to the phase shift. The spectrum of HH 11 shows emission over a large range in velocity, including the highest absolute velocity observed, about -200 km s^{-1} . The shape of the HH 11 profile is sensitive to the position and area of integration, suggesting the presence of velocity structure that cannot be followed on a pixel-to-pixel basis because of the weakness of the emission.

The H₂ profiles for HH 7, 8, 10, and 11 can be compared with the spectra of Zinnecker et al. (1989) which were obtained with an 11" aperture. Our spectra have a higher signal-to-noise ratio, but the general agreement between the two sets of data is good. One difference is that our profiles for HH 8 and HH 10 appear more symmetrical than those of Zinnecker et al.

In order to compare the molecular and atomic gas, [S II] line profiles from Solf & Böhm (1987) are overlaid on the corresponding H₂ profiles in Figure 2. The [S II] profiles cover spatial areas similar to the H₂ ones, except for HH 11 where the optical and H₂ emission do not coincide. The centroid velocities for the H₂ emission are systematically lower (with respect to the cloud rest velocity) than the [S II] velocities by about $20-40 \text{ km s}^{-1}$ throughout the region of HH 7-10. HH 11, which has singularly high (negative) radial velocities in the

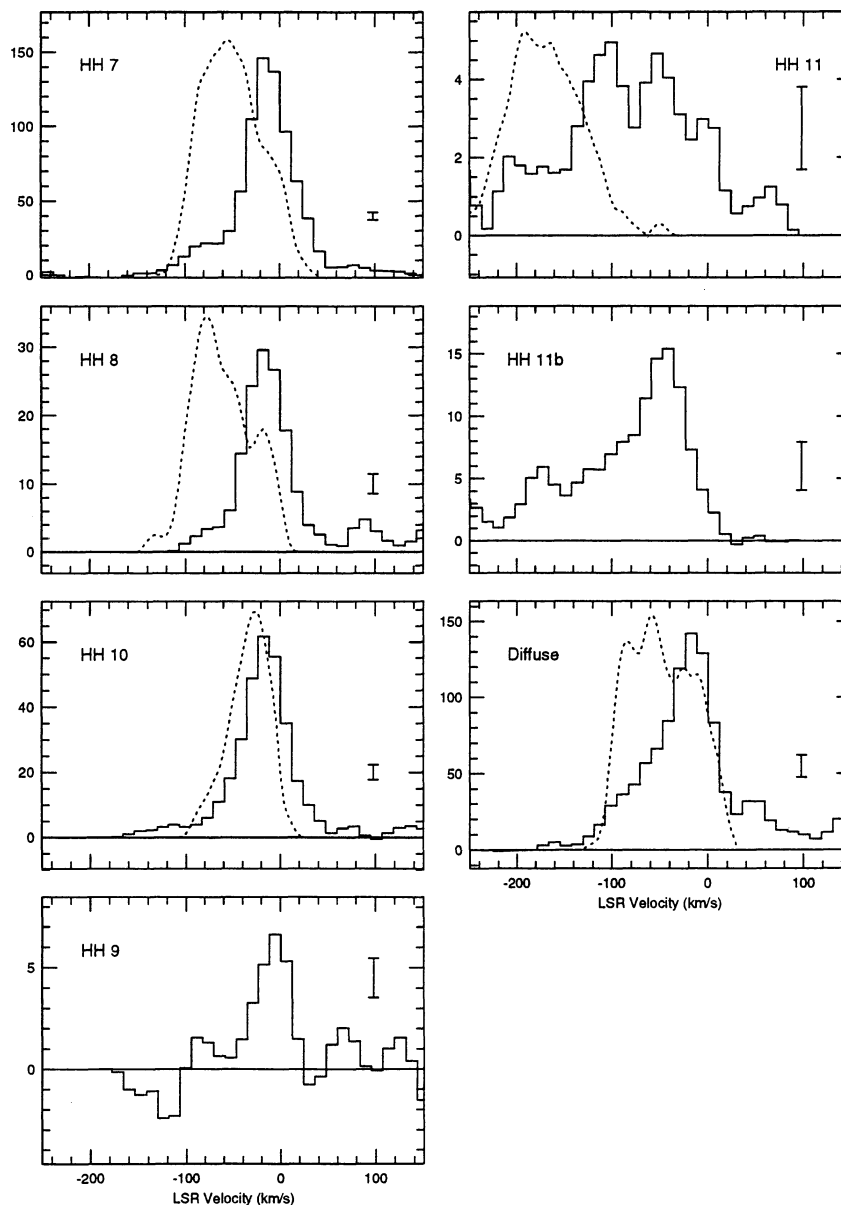


FIG. 2.—Spatially integrated profiles of the 1–0 $S(1)$ line for different regions in HH 7–11. The area covered by each profile is described in the text. The H_2 intensity scale is arbitrary, and each profile has been Hanning smoothed. The dashed lines are $[S\ II]$ line profiles taken from Solf & Böhm (1987) with the intensities scaled with respect to the H_2 profiles.

optical lines is also the region showing the largest absolute H_2 velocities. The H_2 emission always extends to larger positive velocities than does the $[S\ II]$, while the $[S\ II]$ usually, but not always, extends to larger negative velocities. The peaks of the $[S\ II]$ lines tend to coincide in velocity with the H_2 blue wing. One interesting observation is that the full width at zero intensities of the atomic and H_2 lines are comparable, even though the FWHM of the atomic lines is larger.

The spatial coincidence between the H_2 and atomic emission, and the systematic differences between the atomic and molecular velocities leads one to search for a connection between the two. Hartigan et al. (1989) have suggested that the H_2 emission is formed in a magnetic precursor to the J-shock that produces the atomic emission. The neutral gas in a precursor will be gradually accelerated and heated until the disso-

ciating J-front is reached, at which point the temperature and velocity undergo a discontinuity to their postshock values. Hence, for any line of sight through the shock front, the maximum absolute velocity of the molecular gas should be less than that of the atomic gas. The lower absolute peak velocities of the H_2 emission are consistent with this picture, but it should be noted that *the maximum observed velocities are similar to those in the optical lines*. For a bow-shock model, the FWZI velocity of the optical lines is indicative of the bow-shock velocity (Hartigan et al. 1987), about 110 km s^{-1} in this case. The similar FWZI of the H_2 lines indicates that if the H_2 emission is also formed in a bow shock, then similar postshock velocities are reached in the H_2 gas. This statement is not necessarily inconsistent with the precursor picture since only a small fraction of the H_2 intensity is emitted at the high veloc-

ities. We suggest that a portion of the H₂ gas does indeed share the postshock velocity of the atomic gas and is possibly mixed with it, but that the bulk of the H₂ line flux is emitted from a magnetic precursor, or perhaps a preceding C-shock. The postshock H₂ emission could be due to reformation pumping of H₂ (Hollenbach & McKee 1989) or hot H₂ that has survived dissociation in the shock front.

3.2. Velocity Structure of the H₂ Emission

3.2.1. HH 7

HH 7 is the last of the string of HH objects extending from SVS 13 and probably represents the terminus of a collimated jet. The H₂ image of HH 7 shows a bow shock-shaped morphology (Fig. 1). The bow shape is more pronounced in H₂ than it is in the optical lines. The [S II] images also show a distinct secondary emission peak. The eastern peak coincides with the H₂ emission peak, while the western one has been attributed to the Mach disk of the stellar jet (Hartigan et al. 1989; Stapelfeldt et al. 1991).

The line profiles in the central region of HH 7 are shown in Figure 3, in which the spectrum within each 1''/2 pixel is plotted on a spatial grid; the area plotted is defined by the box in Figure 4c. It is immediately obvious that the shapes of the line profiles change remarkably on scales of 1''–2''. Closer examination reveals some systematic patterns in the line profiles. The lines at the intensity peak are broad ($\geq 60 \text{ km s}^{-1}$) and fairly symmetric. Behind the intensity peak (toward SVS 13) the lines are composed of a broad pedestal with a narrow, low-velocity component, and there is a tendency in this region for the lines to be double-peaked. The emission profiles along the northern

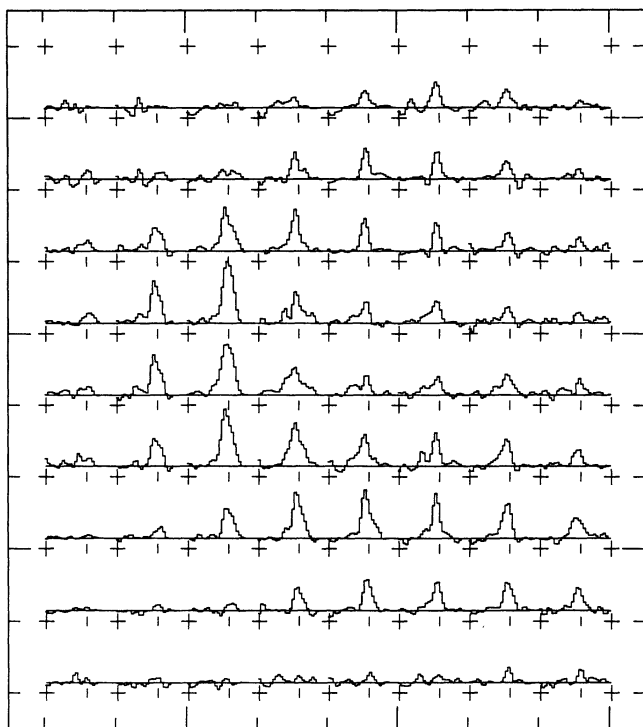


FIG. 3.—The 1–0 S(1) spectra for the central region of HH 7; the area plotted is outlined in Fig. 4c. North is up and east is to the left. Each pixel is 1''/2, and the total velocity extent plotted for each spectrum is 345 km s^{-1} . The spectra have been Hanning smoothed. The vertical tick below each spectrum marks zero LSR velocity.

and southern edge of HH 7 (top and bottom in Fig. 3) are generally narrow with a single velocity component.

Many of the systematics of the velocity field are more easily discerned in the various contour plots presented in Figure 4. Figure 4a is a velocity channel map integrated over the low-velocity emission peak (-24 to 0 km s^{-1}). The low-velocity emission shows a prominent U-shaped ridge and bears a more striking resemblance to a limb-brightened bow-shock shape than does the integrated flux map (Fig. 4c). The high negative velocity emission, however, has a very different spatial distribution. Figure 4b is a contour map of the negative velocity wing (integrated from -95 to -48 km s^{-1}). The high negative velocity emission is localized behind the integrated flux peak within a region defined by the U-shaped ridge of the low (absolute) velocity emission. The high negative velocity gas peaks at a position 1''–2'' behind the total flux peak. The velocity dispersion, defined as the integrated line flux divided by the peak line flux, shows a similar behavior (Fig. 4d): the velocity dispersion is largest behind the total flux peak and decreases toward the edges of the emission region.

Another instructive way of examining the velocity field is with a position-velocity (PV) diagram. Such a diagram is presented in Figure 5; it was constructed using the slit width and position defined in Figure 4c. This figure clearly shows that the negative velocity emission (-50 to -100 km s^{-1}) is confined in the region 1''–4'' behind the intensity peak. In addition, there is a velocity gradient in the negative velocity gas in the sense that the more negative velocities are farthest behind the apex. Strong emission in the positive velocity wing (20 – 50 km s^{-1}) is found only at the apex. The lines become narrow at distances greater than 5'' downstream from the apex. There is also a small gradient in the velocity of the line peak, changing from -18 km s^{-1} at the apex to -5 km s^{-1} downstream.

The above observations are qualitatively consistent with emission from a radiating bow shock. This is readily appreciated by comparing Figure 5 with observed long-slit spectra and calculated PV diagrams for bow-shock models of optical emission lines from HH objects (Böhm & Solf 1985; Raga & Böhm 1986; Hartigan, Raymond, & Meaburn 1990). The PV diagram for the H₂ emission shares the same overall triangular shape, i.e., with the larger velocity dispersion near the apex of the bow shock. The gradient in the negative velocity wing and the spatial separation of the low- and high-velocity peaks are the expected behavior for a bow shock moving at an angle intermediate between the plane of the sky and the line of sight to the observer. The double-peaked lines near the center of HH 7 can be understood as emission from opposite sides of the bow shock, with redshifted emission from receding gas on the far side of the bow shock and blueshifted emission from the side nearest the observer. Those positions away from the bow apex where the line of sight is tangent to the bow-shock surface should show low absolute radial velocities and small velocity dispersion, as is indeed the case (see Figs. 3, 4a, 4d).

As mentioned above, the [S II] images show two emission peaks. The western peak is hypothesized to be the Mach disk in which stellar jet material is shocked. Since the wind is expected to be atomic gas, H₂ emission should not be associated with this shock. The H₂ emission does show two emission peaks when the emission is divided into low- and high-velocity components (Figs. 4a, 4b), with a separation of 1''/5 between the peaks. The second [S II] peak is located farther downstream (about 4'' from the first [S II] peak; Stapelfeldt et al. 1991). Hence, the high-velocity H₂ does not appear to be directly

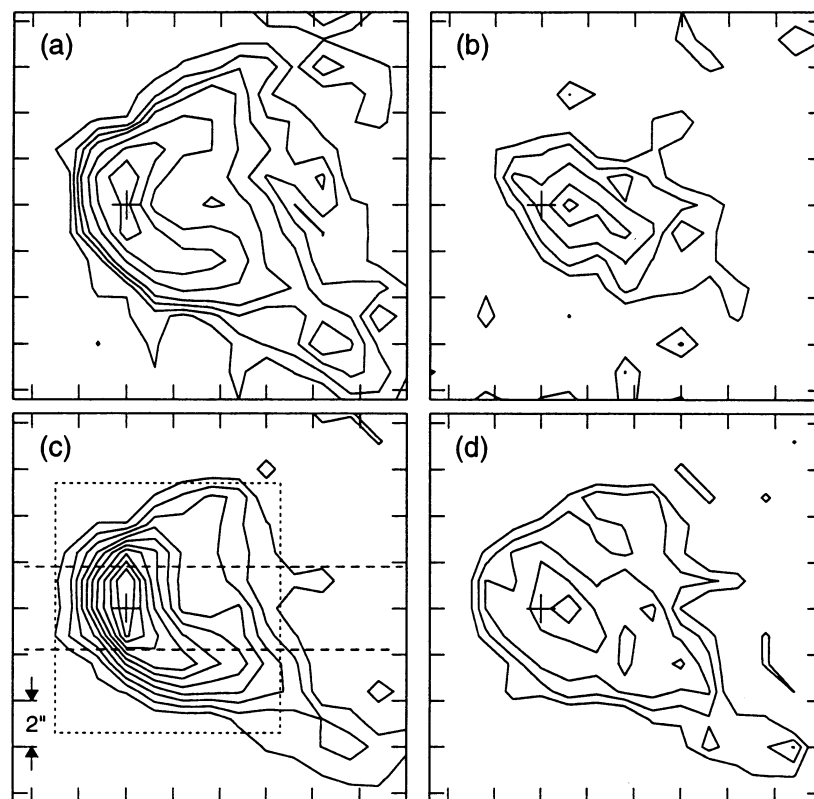


FIG. 4.—Various contour maps for HH 7. The orientation is east to the left and north at the top. The cross marks the position of the peak integrated intensity. (a) Channel map of the 1–0 $S(1)$ emission integrated from -24 to 0 km s^{-1} . Contour levels are 1, 2, 3, 4, 6, 8, 10, $12 \times 2^{1/2} \sigma$. (b) Channel map of the emission in the negative velocity wing integrated from -95 to -48 km s^{-1} . Contour levels are 1, 2, 3, 4, 5 σ . (c) Integrated flux map of HH 7 (as in Fig. 1). The rectangle outlined by the short dashed line indicates the area plotted in Fig. 3. The parallel dashed lines show the slit used to construct the position-velocity diagram in Fig. 5. (d) Map of the velocity dispersion, defined as the integrated line flux divided by the peak line flux. The contour levels are 24, 36, 48, 60, 72 km s^{-1} .

connected with the supposed Mach disk. A detailed comparison of the velocity fields of the H_2 and $[\text{S II}]$ emission in this region would further clarify this issue.

From the morphological shape of HH 7 and the observed velocity field of the gas, we conclude that the H_2 emission is produced in a bow-shock geometry. The PV diagram for the H_2 does look somewhat different than those of the atomic lines in HH 7 (Solf & Böhm 1987), and it differs from theoretically calculated ones for atomic lines in well-resolved bow shocks (Hartigan et al. 1990). In § 4, we will explore further the idea of a bow shock for the molecular gas in HH 7 by calculating some PV diagrams for comparison with the data.

3.2.2. HH 8-11

Only for HH 7, 8, and 10 is the molecular hydrogen emission strong enough to examine the line profiles on a pixel-by-pixel basis. Grids of the emission line profiles for HH 8 and HH 10 are shown in Figure 6. In both cases the signal-to-noise ratio is much lower than for HH 7. The variations in the line profiles are not as dramatic as in HH 7, and unlike HH 7, there are no striking systematic patterns in the velocity field. HH 8 does have a small gradient in the centroid velocity, with the velocities in the northern section more negative by about 12 km s^{-1} .

Figure 7 shows a PV diagram at a position angle of 140° extending from HH 8 to SVS 13. An integrated flux map at this position angle is shown in Figure 7a in which the $6''$ wide slit used for the PV diagram in Figure 7b is defined. The velocities

are approximately constant from HH 8 to HH 10. A small velocity gradient is seen in HH 8, with the absolute value of the velocity decreasing by about 15 km s^{-1} across HH 8. The sense of this gradient is the same as in Solf & Böhm's (1987) PV diagram for the $[\text{S II}]$ line.

The behavior of the gas in the region between SVS 13 and HH 10 is different from that seen in HH 8 and 10. Although no H_2 emission is associated with the peak optical position of HH 11, the H_2 emission does overlap with the western edge of the optical nebulosity (see Stapelfeldt et al. 1991). It may be seen in Figure 7b that the H_2 emission extends over a large range of velocity, as was also found from the spatially integrated profile in Figure 2. Even though the atomic and H_2 emission are not coincident, the two could have a common origin if the observed H_2 emission is from molecular hydrogen reformed behind the HH 11 shock. Hollenbach & McKee (1989) give an equation (their eq. [3.4]) for the distance behind a J shock at which half of the hydrogen is converted to H_2 . Using parameters of $n_0 = 500 \text{ cm}^{-3}$, $v_s = 200 \text{ km s}^{-1}$, and $b = 0.5$ gives a distance of 2.5 , which is similar to the observed separation. The low 1–0 $S(1)$ intensity for HH 11 ($6 \times 10^{-5} \text{ ergs s}^{-1} \text{ cm}^{-2} \text{ sr}^{-1}$, Stapelfeldt et al. 1991) is also consistent with the intensity expected from H_2 recombination pumping (Hollenbach & McKee 1989). The H_2 line ratios produced by recombination pumping are similar to those of UV pumping. Hence, it is possible to test this hypothesis if the line ratios for the faint emission from HH 11 could be measured.

HH 11 shows both the highest atomic and molecular velocities in the HH 7–11 outflow. It is in this same general region

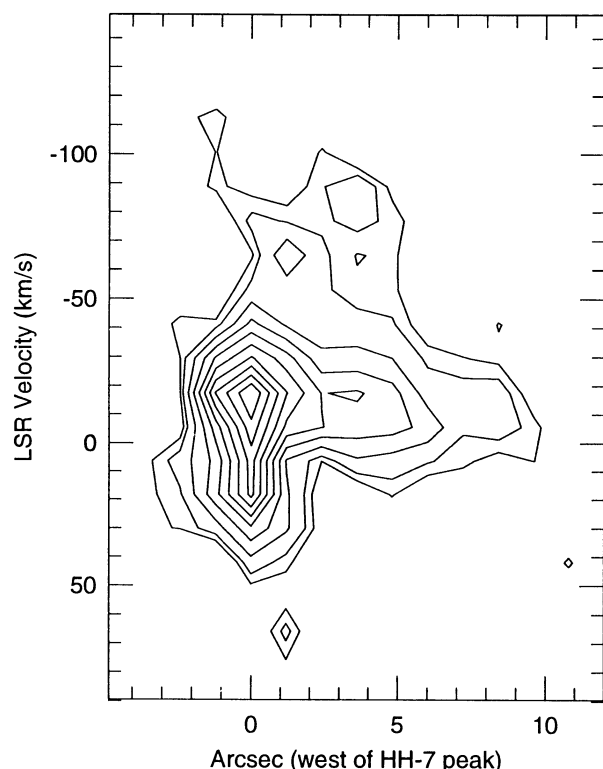


FIG. 5.—Position-velocity diagram for HH 7 using the 3".6 wide slit defined in Fig. 4c. The rest velocity of the molecular cloud is approximately 8 km s^{-1} . The contour levels are 2, 3, 5, 7, 9, 11, 13, 15, 17, 19 σ .

that very large velocities are observed in mm lines of CO (Masson, Mundy, & Keene 1990). Observations in both CO(2–1) and CO(3–2) reveal very high velocity CO emission extending to $\pm 150 \text{ km s}^{-1}$ in the red and blue lobes of the bipolar outflow, respectively. This high-velocity CO emission is very spatially localized. One of the “knots” of CO emission is located in the region between HH 11 and SVS 13 and has a velocity peak at -100 km s^{-1} . It is interesting that all of the high-velocity tracers in the optical, infrared, and millimeter are concentrated in the same region (at least in the blue outflow). Unfortunately, the 21" radio beam does not permit a more detailed comparison of the spatial distribution.

The CO gas appears to be much cooler ($< 100 \text{ K}$) than that expected for thermal H₂ emission (Masson et al. 1990), but H₂ recombination emission behind a shock would originate in a region of cool gas (Hollenbach & McKee 1989). Whether the high-velocity CO emission could also originate from gas in a molecular recombination region after passing through a high-velocity shock is worth considering. Intensities for the CO ($J = 3-2$) line as given by Hollenbach & McKee (1989) fall in the range of 10^{-6} to $10^{-5} \text{ ergs s}^{-1} \text{ cm}^{-2} \text{ sr}^{-1}$ for shock velocities greater than 50 km s^{-1} with $n_0 = 10^3 \text{ cm}^{-3}$. This translates to 10^3 to $10^4 \text{ Jy km s}^{-1}$, which is within a factor of a few to the integrated fluxes observed in the very high velocity gas by Masson et al. (1990). The position of peak intensity in the high-velocity CO emission, however, does not coincide with the H₂ emission, but the difference is within the pointing uncertainty of the radio measurements.

4. BOW-SHOCK MODEL FOR HH 7

Bow-shock models have enjoyed reasonable success in explaining observed line profiles, velocity fields, and line ratios

for atomic emission lines in some HH objects (Raga & Böhm 1986; Hartigan et al. 1987; Hartigan et al. 1990). In such models, each point on the bow surface is treated as an oblique shock, with the simplification that the emission at that point can be described by a planar shock model with shock velocity equal to the component of the bow-shock velocity normal to the surface. Given the bow-shock shape, the orientation, and a set of planar shock models for different shock velocities, it is then possible to calculate integrated line profiles, long-slit spectra, or maps of line profiles (see Hartigan et al. 1987). In principle, bow-shock models may be calculated for H₂ emission if grids of appropriate planar shock models are available. The calculation of bow-shock models for either C-shocks or J-shocks with magnetic precursors would, however, be more complicated than for J-shocks because each point on the bow shock can no longer be described by a single intensity and radial velocity, since C-shocks or precursors have a finite length over which the gas emissivity and velocity vary. In addition, the introduction of additional variables (the ionization fraction, and the magnetic field strength and orientation) increases the parameter space. The type of shock proposed for HH 7, a J-shock with a magnetic precursor, is a complicated computational problem, and the detailed calculations required for inclusion in theoretical bow-shock models are not yet available.

In order to explore the velocity field in HH 7, PV diagrams were calculated by parameterizing the expected behavior of the important variables in a magnetic precursor. We start with the assumption that the H₂ emission is comprised of two components: high-velocity postshock H₂, and H₂ in a magnetic precursor. The postshock emission is assumed to be formation pumping where the intensity as a function of shock velocity for a 10^3 cm^{-3} gas is given by Hollenbach & McKee (1989). The calculations for this component can proceed in the same manner as for atomic lines in a dissociative shock (e.g., Hartigan et al. 1990), ignoring the fact that the H₂ will reform at a finite distance downstream from the shock front.

The neutrals in a precursor are gradually heated and accelerated. In order to calculate a bow-shock model, the H₂ emissivity as a function of velocity in the precursor must be known for each shock velocity. The maximum velocity of the neutrals in the precursor is set equal to a fixed fraction of the shock velocity, $v_{\text{max}} = k_v v_s$, and the velocity is assumed to increase linearly from zero to the maximum velocity. The temperature is also assumed to increase linearly from zero to a maximum temperature. The maximum temperature is taken to be a power law of the shock velocity, normalized to match the maximum kinetic temperature at $v_s = 50 \text{ km s}^{-1}$ in the C-shock model of Draine, Roberge, & Dalgarno (1983; their Fig. 8a), giving $T_{\text{max}} = 3300(v_s/50)^a$. To account for the fact that the H₂ population is likely to be in non-LTE, the excitation temperature is approximated by $T_{\text{ex}} = bT_k$, where $b < 1$. The precursor length is taken to be constant along the bow shock; this will be true only if the bow-shock velocity is perpendicular to the magnetic field direction. The physical value of the precursor length does not enter into the calculation, though it is assumed to be much smaller than the bow-shock size. The precursor is then parameterized by the variables k_v , a , and b .

The remaining variables required to describe the bow-shock model are the bow-shock velocity v_{bs} , the observed orientation ϕ , and the shape of the bow shock. A bow-shock velocity of about 100 km s^{-1} and an orientation angle of $\phi \leq 45^\circ$ are indicated by the profiles of the optical emission lines (Hartigan et al. 1987). The shape of HH 7 in the H₂ images is fitted well

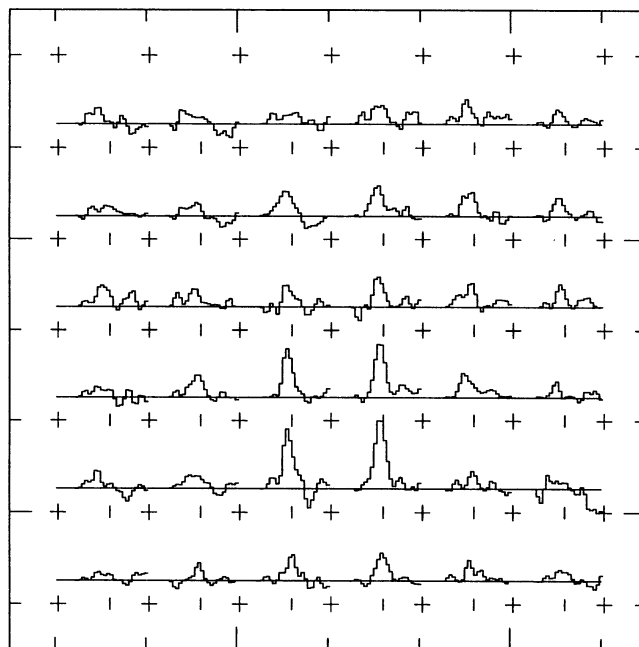


FIG. 6a

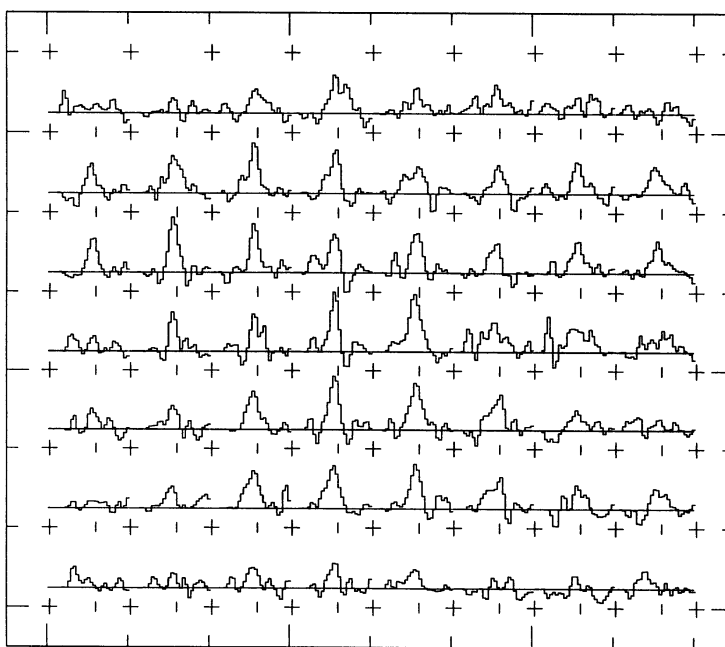


FIG. 6b

FIG. 6.—Same as Fig. 3, but 1–0 $S(1)$ spectra for the regions centered on (a) HH 8 and (b) HH 10

by shapes of the form $z = Ar^2 + Br^4$ as used by Hartigan et al. (1987), and this general shape was used to investigate the PV diagrams. The PV diagrams were constructed for an infinitely narrow slit in order to simplify the calculations. The two emission components, the postshock and the precursor, were calculated separately and then scaled in intensity to match the relative intensities observed in the low- and high-velocity components. The calculated PV diagrams were smoothed in the spatial direction with a seeing function and in velocity with a 25 km s^{-1} Lorentzian.

The orientation angle, the bow-shock velocity, and the shape of the bow shock were first determined by fitting the shape of the negative velocity wing, which is emitted by the postshock component. The best values for these parameters were $v_{\text{bs}} = 100 \text{ km s}^{-1}$, $\phi = 35^\circ$, and a shape given by $A = 0.07$ and $B = 0.0046$. Then the parameters for the precursor component were adjusted to provide the best possible match to the emission at the leading edge and along the lower velocity ridge. Figure 8 shows one calculated PV diagram that bears a good resemblance to the observed one. The parameters for the plot

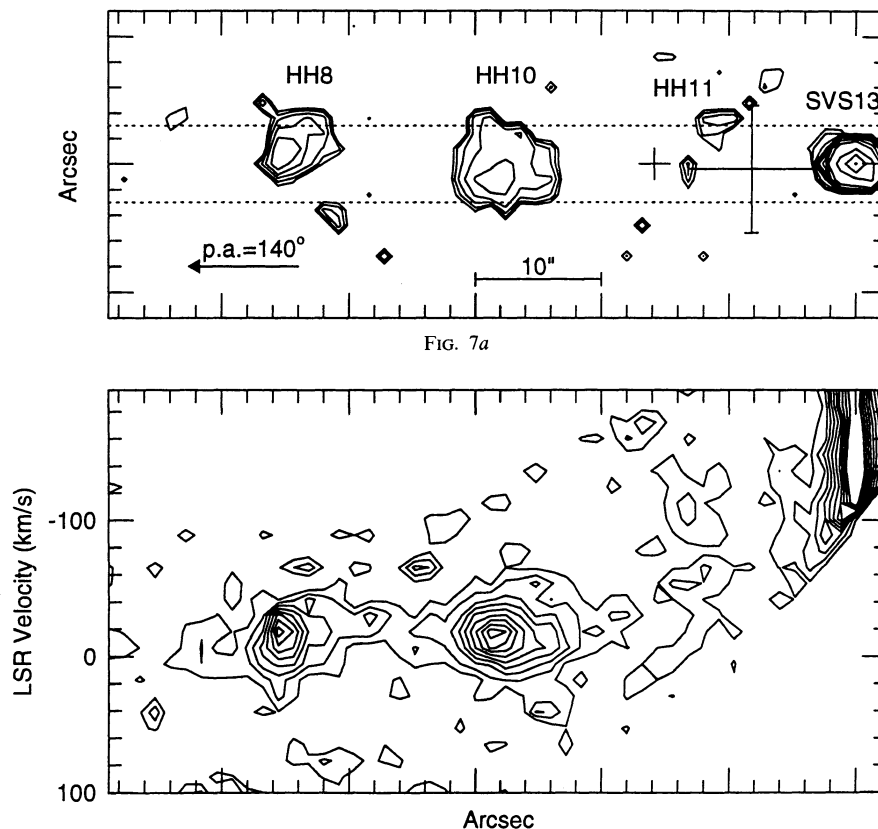


FIG. 7a

FIG. 7b

FIG. 7.—(a) Upper panel is the integrated flux map of the 1–0 $S(1)$ emission for a strip from SVS 13 to HH 8 at a position angle of 140° . The small cross marks the position of peak intensity in the optical for HH 11. The large error bars show the position and uncertainty for the peak intensity of the extremely high velocity gas observed in CO (3–2) by Masson et al. (1990). The dotted lines show the slit for the PV diagram. (b) Lower panel is the PV diagram from SVS 13 to HH 8. The contour levels are 1, 2, ..., 10, 15, 20 σ . Note the gap in the lower right-hand corner (where the continuum from SVS 13 is cut off) and the upper left-hand region due to the limits of the velocity coverage.

in Figure 8 are $k_v = 0.35$, $a = 0.6$, and $b = 0.55$. With these values, the neutrals reach a maximum velocity of 35 km s^{-1} and a maximum kinetic temperature of 5000 K at the apex of the bow shock. This model reproduces the general shape of the observed PV diagram, with the exception that the position of peak intensity in the observed PV diagram at -15 km s^{-1} is not matched. The data also have a longer tail than does the model; this emission may be due to lower velocity ($< 50 \text{ km s}^{-1}$) C-shocks which are not included in the calculations.

5. DISCUSSION

The most important result of this paper is that the velocity field of the H₂ emission in HH 7 is that expected for a bow-shock structure. This is particularly clear for the high-velocity negative wing, which is well described by a postshock emission component with an orientation angle of $\sim 35^\circ$ and a bow-shock velocity of about 100 km s^{-1} . The low absolute velocity emission has been represented in this paper as a magnetic precursor to a J-shock, though this is not yet firmly established.

Smith & Brand (1990) have calculated H₂ line profiles for C-shocks in high-velocity bow shocks. In their models the H₂ emission is restricted to regions on the bow-shock surface where the effective shock velocity is less than the break-down velocity, about 45 km s^{-1} . Their typical 120 km s^{-1} bow-shock model has a dissociative J-shock at the bow apex and C-shocks

in the wings of the bow shock which produce the H₂ emission. None of their calculated profiles has FWHM velocities greater than about 12 km s^{-1} . These widths are far too narrow to explain the line width of the integrated profile for HH 7 ($\sim 40 \text{ km s}^{-1}$ deconvolved) and, indeed, those of a number of HH objects (Zinnecker et al. 1989). The reason for the narrow lines is that most of the emission in the C-shocks is produced near the molecular cloud velocity, since the gas has cooled substantially by the time it has accelerated to the full shock velocity. For the same reason, the C-type bow shocks fail to explain the observed shift of about -20 km s^{-1} in the H₂ profiles of HH 7, 8, and 10; similar velocity shifts are observed in the H₂ profiles of other HH objects (Zinnecker et al. 1989). In addition, a model with a dissociative shock at the apex and H₂ emission only in the wings does not fit the observed images or the PV diagram for HH 7. Because H₂ emission would be absent at the projected bow apex, for $\phi \sim 35^\circ$ the intensity map should show a hole of decreased H₂ emission just behind the leading edge (Smith 1991) with the intensity increasing again farther downstream: similarly, the PV diagram would be doubled-peaked along the slit. This is not observed; rather, the images show a limb-brightened arc with a steady decrease in intensity downstream.

Perhaps the soft C-shocks proposed by Smith, Brand, & Moorhouse (1991) could explain the H₂ emission in HH 7. These shocks can accelerate neutrals to high velocities without

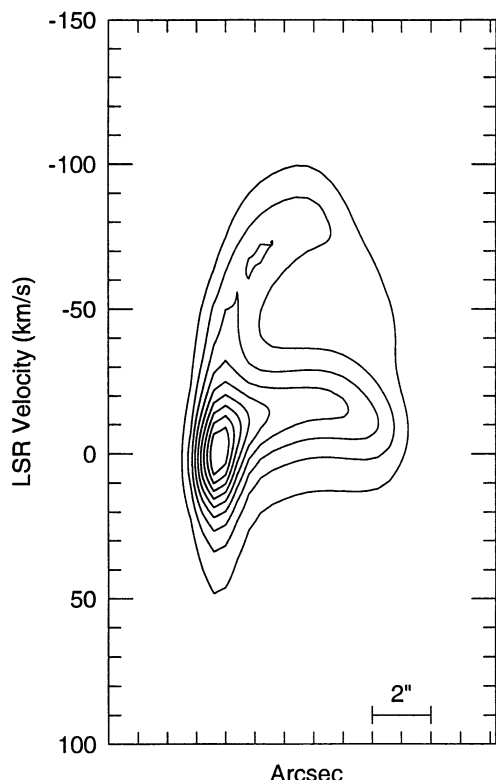


FIG. 8.—Theoretical PV diagram for HH 7 calculated with the model and parameters described in the text.

dissociating H_2 in shocks as fast as 130 km s^{-1} and are able to produce line widths up to 40 km s^{-1} with a 250 km s^{-1} bow shock in a gas with density of $3 \times 10^6 \text{ cm}^{-3}$ and a field of 0.05 G . Calculations of the velocity fields for such bow shocks would be of interest. However, these types of shocks require extremely high magnetic fields, which may not be found in the relatively low densities expected in the vicinity of HH 7.

The reason that the magnetic precursor model in the current paper succeeds in reproducing the H_2 velocity field is that the H_2 emissivity increases with velocity in the precursor. Hence, the H_2 emits over a range of velocities but peaks near the maximum velocity in the precursor. This results in larger line widths than a pure C-shock model and produces a shift in the peak velocity for $\phi < 90^\circ$. A J-shock with a magnetic precursor is an attractive explanation for a number of other reasons. It has the potential to explain simultaneously the atomic and H_2 line emission and their close spatial coincidence, and it is able to account for the presence of H_2 emission at the apex of a bow shock with shock velocities $\sim 100 \text{ km s}^{-1}$. Magnetic precursors may also explain the discrepancy between the very low excitation nature of HH 7 and other low-excitation HH objects

(effective shock velocity $< 50 \text{ km s}^{-1}$) and large atomic line widths ($\geq 100 \text{ km s}^{-1}$), if it can be demonstrated that the magnetic precursors can carry away a large enough fraction of the shock energy.

Curiel (1992) has also calculated H_2 (and atomic) line profiles and PV diagrams for bow shocks with a J-shock plus magnetic precursor. His simplified model for the precursor differs from the one in this paper in that the actual H_2 level population is calculated and the maximum temperature of the neutrals is determined by calculating the H_2 cooling. The differences between his calculated PV diagram for HH 7 and the one in this paper can probably be traced to the higher precursor temperatures in his model with a stronger dependency of the maximum temperature on shock velocity.

A crucial question for the precursor scenario is whether magnetic precursors producing strong H_2 emission can exist at shock velocities $\sim 100 \text{ km s}^{-1}$. The properties and existence of magnetic precursors in molecular gas need to be established by detailed computational modeling. The theoretical PV diagram presented in this paper (Fig. 8) is able to reproduce the essential features of the observed H_2 velocity field, but it is based on a parameterized model for the precursor which lacks a computational basis. However, the model does indicate that the magnetic precursor scenario is a promising explanation for the emission in HH 7, and perhaps other HH objects, if magnetic precursors in molecular gas behave in a similar fashion.

The future looks promising for testing models of H_2 emission in HH objects and other interstellar shocks, including J-shocks with magnetic precursors. Long-slit spectra of H_2 lines can now be obtained with both high-velocity resolution and high spatial resolution using infrared echelle spectrographs. Such data could, for example, discriminate between a C-shock and a magnetic precursor by comparing high- and low-excitation lines: the high-excitation lines in a pure C-shock should arise at velocities close to the rest velocity where the temperature peaks, while in a magnetic precursor they would form preferentially at the higher velocities in the precursor. Since both the temperature and velocity vary throughout a magnetically mediated shock, long-slit spectra of selected H_2 lines can essentially begin to dissect the shock structure. Combined with similar quality optical or infrared data on atomic lines, such data will provide challenging constraints for models of HH objects.

It is a pleasure to thank J. Bland who gave generously of his time and knowledge of Fabry-Perot imaging. I thank Tom Geballe and the staff of UKIRT for support of these observations. The UKIRT is operated by the Royal Observatory Edinburgh on behalf of the UK Science and Engineering Research Council. This work was conducted while the author was supported by NSF grant AST 86-15906 at the Institute for Astronomy, University of Hawaii.

REFERENCES

- Bland, J., & Tully, R. B. 1989, *AJ*, 98, 723
 Böhm, K. H., & Solf, J. 1985, *ApJ*, 294, 533
 ———. 1990, *ApJ*, 348, 297
 Curiel, S. 1992, Ph.D. thesis, Instituto de Astronomía, Universidad Nacional Autónoma de México
 Draine, B. T., Roberge, W. G., & Dalgarno, A. 1983, *ApJ*, 264, 485
 Elias, J. H. 1980, *ApJ*, 241, 728
 Hartigan, P., Curiel, S., & Raymond, J. 1989, *ApJ*, 347, L31
 Hartigan, P., Raymond, J., & Hartmann, L. 1987, *ApJ*, 316, 323
 Hartigan, P., Raymond, J., & Meaburn, J. 1990, *ApJ*, 362, 624
 Hollenbach, D. J., Chernoff, D. F., & McKee, C. F. 1989, in *Infrared Spectroscopy in Astronomy*, ed. B. H. Kaldeich (Paris: ESA), 245
 Hollenbach, D., & McKee, C. F. 1989, *ApJ*, 342, 306
 Masson, C. R., Mundy, L. G., & Keene, J. 1990, *ApJ*, 357, L25
 Raga, A. C., & Böhm, K. H. 1985, *ApJS*, 58, 201
 ———. 1986, *ApJ*, 308, 829
 Schwartz, R. D., Cohen, M., & Williams, P. M. 1987, *ApJ*, 322, 403
 Schwartz, R. D., Williams, P. M., Cohen, M., & Jennings, D. G. 1988, *ApJ*, 334, L99
 Smith, M. D. 1991, *MNRAS*, 252, 378
 Smith, M. D., & Brand, P. W. J. L. 1990, *MNRAS*, 245, 108
 Smith, M. D., Brand, P. W. J. L., & Moorhouse, A. 1991, *MNRAS*, 248, 730
 Solf, J., & Böhm, K. H. 1987, *AJ*, 93, 1172
 Stapelfeldt, K. R., Beichman, C. A., Hester, J. J., Scoville, N. Z., & Gautier, T. N. 1991, *ApJ*, 371, 226
 Wilking, B. A., Schwartz, R. D., Mundy, L. G., & Schultz, A. S. B. 1990, *AJ*, 99, 344
 Zinnecker, H., Mundt, R., Geballe, T. R., & Zealey, W. J. 1989, *ApJ*, 342, 337